Chiral-bubble-induced topological Hall effect in ferromagnetic topological insulator heterostructures

Wenbo Wang,[1,2,*] Yi-Fan Zhao,[3] Fei Wang,[3] Matthew W. Daniels,[4] Cui-Zu Chang,[3] Jiadong Zang,[5] Di Xiao,[6] and Weida Wu[2,†]

[1]*Department of Physics, University of California, Santa Barbara, CA 93106, USA*
[2]*Department of Physics and Astronomy, Rutgers University, Piscataway, NJ 08854, USA*
[3]*Department of Physics, The Pennsylvania State University, University Park, PA 16802, USA*
[4]*Alternative Computing Group, National Institute of Standards and Technology, Gaithersburg, MD 20899, USA*
[5]*Department of Physics and Materials Science Program, University of New Hampshire, Durham, NH 03824, USA*
[6]*Department of Physics, Carnegie Mellon University, Pittsburgh, PA 15213, USA*

(Dated: September 15, 2020)

We report compelling evidence of emergent THE from chiral bubbles in a two-dimensional uniaxial ferromagnet, V-doped Sb_2Te_3 heterostructure. The sign of THE signal is determined by the net curvature of domain walls in different domain configuration, and the strength of THE signal is correlated with the density of nucleation or pinned bubble domains. The experimental results are in good agreement with the integrated linear transport and Monte Carlo simulations, corroborating the emergent gauge field at chiral magnetic bubbles. Our findings not only reveal a general mechanism of THE in two-dimensional ferromagnets, but also pave the way for the creation and manipulation of topological spin textures for spintronic applications.

It is of fundamental interest to understand the quantum transport of quasiparticles under an emergent gauge field in strongly correlated systems [1–4]. The topological Hall effect (THE) originates from the emergent gauge field of non-coplanar spin textures in real space. It has been utilized as a powerful probe for detecting exotic magnetic phases, such as skyrmion lattices in chiral magnets [5–8] and possible spin liquid orders[4]. The recent observation of the THE above the Curie temperature in two-dimensional (2D) ferromagnets provides strong evidence that spin chirality fluctuations emerge in a ferromagnet with weak Dzyaloshinskii-Moriya interaction (DMI) [9]. In such systems, the DMI energy D is less than the critical value $D_c \equiv 2\sqrt{2JK}/\pi$ (J and K are Heisenberg exchange and uniaxial anisotropy energy terms) needed to stabilize a non-coplanar ground state. Nevertheless, this weak DMI can induce chirality in the spin excitations, though it is unclear whether weak DMI plays a role in topological objects, such as domain walls, in the ordered state.

Experimentally, the THE has also been observed in various ferromagnetic ultrathin films and heterostructures well below the Curie temperature ($T \ll T_c$) [10–13]. At such low temperatures, thermal fluctuation is suppressed, and thus cannot be responsible for the observed THE. Therefore, the THE in these systems originates from static spin textures—despite their subcritical DMI. The typical magnetization reversal process of a ferromagnet involves domain nucleation and domain wall propogation. In centrosymmetric ferromagnets, spins along ferromagnetic domain walls rotate without preferred handedness. However, broken inversion symmetry at the interface in heterostructures can lift this chiral degeneracy through the DMI, leading to chiral domain walls in ultrathin film systems and 2D ferromagnets [14, 15]. The fact that the THE in these systems is observed in the vicinity of the coercive field indicates that chiral domain walls, instead of skyrmion lattices, are likely the driving force. When electrons pass through curved chiral domain walls, they experience an effective magnetic (gauge) field due to a real-space Berry curvature that is proportional to the solid angle subtended by the three neighboring spins (a spin triad) [2, 3, 9]. Magnetic bubbles enclosed by these chiral domain walls are often called chiral (skyrmion) bubbles [16], which carry the same topological charge (TC) as skyrmions. Skyrmions stabilized by DMI merely have a single spin in the center pointing opposite to the spins outside of the skyrmion, whereas chiral bubbles can have extended uniformly magnetized regions on their interior.

In typical ferromagnets, the magnetization reversal process starts with domain nucleation. The first peak of the THE appears when these nucleation bubble domains proliferate. The reversed domains expand and coalesce into larger domains with further increase of the external magnetic field. Once the majority of the magnetization is reversed, some unreversed bubbles remain pinned. Those pinned bubbles have opposite central magnetization compared to bubbles at the nucleation stage, and thus lead to a second peak in the THE with opposite sign [17]. However, previous works usually report only one peak, either a "hump" or "dip" in anomalous Hall effect (AHE) loops during magnetization reversal, which is considered as hallmark of the THE [10–13, 18]. On the other hand, these features could be trivially attributed to addition of two AHE contributions with different coercivities and opposite signs[19–21]. In order to unequivocally extract the intrinsic THE and investigate the necessary existence of the chiral bubble state, the anomalous Hall signals have to be either accurately characterized or entirely suppressed, which is experimentally challenging. Usually one assumes the AHE is proportional to magnetization, the measurement of which requires a highly sensitive magnetometer for 2D magnets.

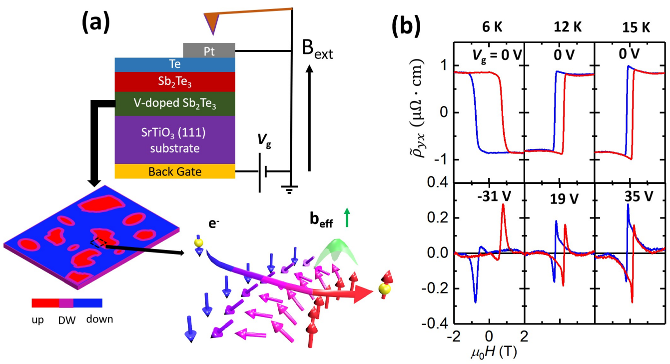

FIG. 1. (a) A schematic of the Sb_2Te_3/V-doped Sb_2Te_3 bilayer grown on $SrTiO_3$ (111) capped by 10 nm Te. A layer of Pt is grown on top for MFM measurements. The potential between the magnetic tip and Pt layer is balanced to eliminate the electrostatic interaction. A back-gate voltage V_g is applied to tune the anomalous Hall effect (AHE). Magnetic fields are applied perpendicular with film. The non-coplanar spins on the curved chiral domain walls (DW) carry topological charges, which behave as effective magnetic fields b_{eff} in real space. An electron, passing through the curved chiral domain wall, will experience b_{eff} and deflect by an emergent Lorentz force. (b) the Hall resistivity $\tilde{\rho}_{yx}$ (with the ordinary Hall effect subtracted out) as a function of magnetic field H at various temperatures from 6 K to 15 K. The top row shows $\tilde{\rho}_{yx}$ with $V_g = 0$. Bottom row shows the intrinsic THE when a back-gate voltage is applied to zero the AHE.

Here, we report the observation of a chiral-bubble-induced THE in a V-doped Sb_2Te_3 (VST) heterostructure where the AHE background can be tuned to zero with a back-gate voltage. Both positive and negative THEs have been observed during the magnetization reversal process, which are correlated with nucleation and pinned bubble domains visualized by cryogenic magnetic force microscope (MFM). The emergent gauge field at chiral bubbles was confirmed by Monte Carlo simulations. The integrated transverse response to the gauge field was reproduced by Kubo formula calculation of a tight-binding model. All together, our results provide compelling evidence of chiral bubbles as a common origin of the THE in 2D ferromagnets.

Fig. 1(a) shows a cartoon schematic of the VST heterostructure and device configuration for MFM studies. A five-quintuples (QL) VST thin film capped with 3 QLs Sb_2Te_3 (ST) was grown on a $SrTiO_3$ substrate. A layer of 15 nm Pt was deposited on the surface of the sample to eliminate electrostatic interaction during MFM measurements. The charge transfer between the ST layer and

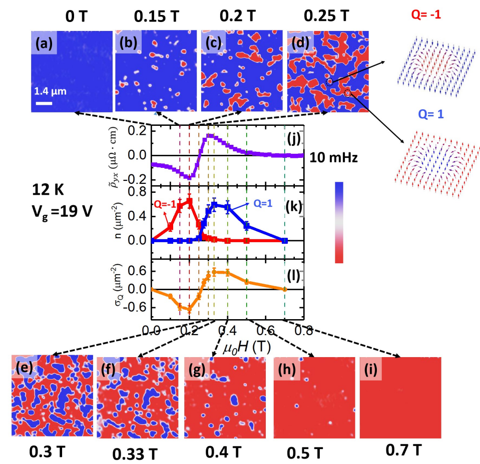

FIG. 2. (a)-(i) MFM images measured at 12 K and $V_g = 19$ V as magnetic field is swept from 0 T to 0.7 T. The film was first saturated at -2 T. At 0.25 T, the MFM image shows both nucleation bubbles and pinned bubbles, which respectively carry $Q = -1$ and $Q = 1$ topological charge (TC). Schematic pictures of the spin textures of these topological bubbles are shown. (j) Hall resistivity $\tilde{\rho}_{yx}$ (with the OHE subtracted out) at various magnetic fields; standard deviation error bars are smaller than the data points. (k) density (n) of magnetic bubbles (red for $Q = -1$ bubbles and blue for $Q = 1$ bubbles) at various magnetic fields, based on the chosen MFM image; error bars give the sample standard deviation due to our finite area sampling. (l) the density (σ_Q) of TC as a function of magnetic fields; error bars are again sample standard deviation. The field-dependence of σ_Q shows the similar behavior as the topological Hall resistance (j).

VST layer can lift the Fermi level of the VST layer closer to band crossing or anti-crossing points [21]. A back-gate voltage was applied to fine tune the Fermi level across these points, resulting in a sign change of the AHE. More importantly, the AHE in this sample can be tuned to zero over the entire temperature range studied here, which allows an unambiguous isolation of the THE signal [9, 22]. In general, there are three contributions to the Hall resistivity in a magnetic metal: the ordinary Hall effect (OHE) proportional to H, the conventional AHE proportional to the magnetization M, and the THE due to the real-space Berry phase [5, 7, 8]. We can therefore express the Hall resistivity as $\rho_{yx}(H) = R_0 H + R_S M + \rho_H^{\mathrm{T}}$. The contribution from the OHE can be easily separated out from the slope at high magnetic field. Here we focus on the anomalous part: $\tilde{\rho}_{yx} \equiv \rho_{yx} - R_0 H$.

As shown in Fig. 1(b), square-like hysteric loops of $\tilde{\rho}_{yx}(H)$ are observed below the transition temperature (T_{C}), which indicates a robust ferromagnetism with perpendicular magnetic anisotropy (PMA). At 12 K and 15 K, the THE signal can be directly inferred from the humps in $\tilde{\rho}_{yx}(H)$ loops. This hump feature is absent at 6 K, suggesting the absence of THE. Nevertheless, when the back-gate voltage is applied to suppress the AHE, clear topological Hall signals are revealed at all three temperatures. These results demonstrate that the existence of a THE cannot be simply inferred from the shape of the anomalous Hall loop, especially when the AHE signal overwhelmingly dominates. Furthermore, both positive and negative THE signals are observed, indicating the existence of both negative and positive topological charges. These topological charges survive at higher temperatures, even above T_c [9, 22], indicating a crossover from static chiral spin textures to dynamic ones.

MFM images taken simultaneously with the *in-situ* transport measurements are shown in Figure 2. The field-dependent MFM images obtained during the magnetization reversal at 12 K show typical ferromagnetic behavior with one-step switching[23, 24]. Therefore, the topological Hall features are unlikely due to the superposition of two AHE loops with different cercivities and opposite signs[20], further corroborating the intrinsic mechanism of emergent gauge field from chiral spin textures. Each closed domain wall carries an integer number of TCs, independent of the length and the shape of the domain walls. Since the MFM technique is unable to resolve the spin textures, it is hard to determine the topological number of each chiral bubble. Here we simply assume that each bubble in an MFM image carries a single TC: $Q = \pm 1$. The negative THE signal reaches a maximum around 0.2 T, which correlates with the highest density of nucleation bubbles (red) observed in MFM images. Similarly, the positive THE signal reaches its maximum around 0.3 T which correlates with the highest density of pinned bubbles (blue). The nucleation ($Q = -1$) and pinned ($Q = 1$) bubbles have opposite magnetization but the same chirality, and therefore carry opposite TCs.[17] The $Q = -1$ and $Q = 1$ bubbles coexist equally at $\mu_0 H_c \approx 0.25$ T, and thus the net TC is zero at that point. Consistent with the TC density, the THE approximately reaches zero at $\mu_0 H_c$. The density of $Q = -1$ and $Q = 1$ bubbles within the 7×7 μm^2 scanned area are plotted in Fig. 2(k)[22, 25]. The field dependence of the net topological charge density (orange curve) qualitatively agrees well with the *in-situ* topological Hall signals (purple curve), providing strong evidence for the topological charges carried by the chiral bubbles. Note that finite THE still exists at zero magnetic field, while no magnetic bubbles are visible in MFM image. This indicates the remnant fluctuation-driven THE still exists at 12 K ($\approx 0.44 T_c$) because of significant thermal excitation. On the other hand, the dynamical fluctuation is absent at 6 K, consistent with the suppression of thermal fluctuation[9]. The estimated topological Hall resistance from TC density is roughly 10% of the value from transport measurement[22]. The underestimation of the THE from MFM images can be ascribed to the limited MFM lateral resolution and possibility of multiple TCs carried by a single magnetic bubble.

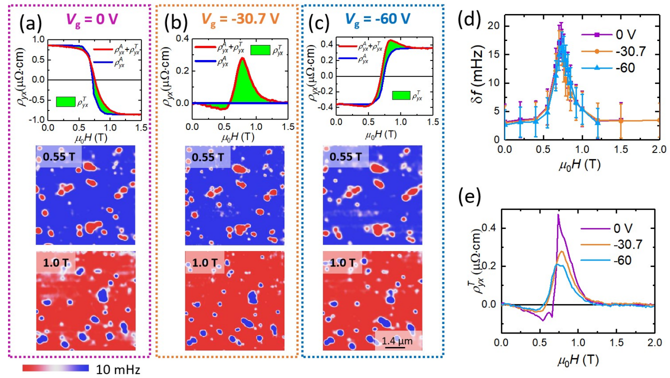

FIG. 3. (a) $\tilde{\rho}_{yx} = \rho^{\mathrm{A}}_{yx} + \rho^{\mathrm{T}}_{yx}$ (red) of VST film at 6 K and $V_{\mathrm{g}} = 0$ V. Anomalous Hall signal ρ^{A}_{yx} (blue) are estimated from the MFM images. The difference between $\tilde{\rho}_{yx}$ and ρ^{A}_{yx} is the topological Hall signal ρ^{T}_{yx} (green area). The MFM images measured at 0.55 T and 1.0 T show the local distribution of nucleation bubbles and pinned bubbles. (b),(c) the Hall signals and MFM images of VST at $V_{\mathrm{g}} = -30.7$ V and $V_{\mathrm{g}} = -60$ V. The MFM images were taken exactly at the same region. The nucleation bubbles and pinned bubbles measured at same magnetic fields are observed at similar locations. (d) The field dependence of the standard deviation of MFM images (δf) measured at $V_{\mathrm{g}} = 0$, -30.7 V, and -60 V are almost identical; error bars are the standard deviations of δf in the single-domain state. (e) ρ^{T}_{yx} at $V_{\mathrm{g}} = 0$ V, -30.7 V, and -60 V shows similar field dependence with a small dip and a large peak.

At 6 K, the THE becomes notably asymmetric between its positive and negative peaks, as shown in Fig. 3(a)-(c). At $V_g = V_g^0 = -31$ V, the AHE is zeroed. Tuning the back-gate voltage away from V_g^0 leads to a finite AHE contribution, which overwhelms the THE signals. For instance, at $V_g = 0$ V, the Hall signal (with the OHE subtracted out) $\tilde{\rho}_{yx}$ shows a ferromagnetic hysteresis behavior, without any sign of a THE. However, the anomalous Hall loop $\rho^A_{yx}(H)$ inferred from the magnetization loop using MFM measurements [22] does not agree with the $\tilde{\rho}_{yx}(H)$ loop from transport measurements. The difference between them, indicated by the green area, is the topological Hall signal (ρ^T_{yx}) [9]. Similar THE signal is also observed at $V_g = -60$ V, where the sign of the AHE changes. Although the AHE shows a strong gate dependence, the ferromagnetic domain behavior shows little change. Quantitatively, the root-mean-square values of MFM images (scaled with the stray field strength) at various magnetic fields are independent of the back-gate voltages, as shown in Fig. 3(d) [22]. This demonstrates that the relatively small change in the charge carrier density has little influence on the ferromagnetism of the VST film mediated by the Ruderman-Kittel-Kasuya-Yosida (RKKY) interaction. Moreover, the magnetic domain structures show similar patterns. At 0.55 T and 1.0 T, the nucleation domains (red) and pinned domains (blue) at different back-gate voltages form at similar locations, indicating that these are very likely to be disorder sites [22]. The nucleation sites are likely to have lower exchange energy J and lower anisotropy K, while the pinned sites are likely to have stronger J and K. The THE signals at three different back-gate voltages show essentially the same field dependence with only slight variations in magnitude, which may arise from the imperfect subtraction of the AHE loop using MFM results. The differing gate dependence of the THE and the AHE indicate different physical origins. The AHE originates from the momentum-space Berry curvature, which is sensitive to the Fermi level [21]; the THE originates from the emergent gauge field of real-space spin textures , which is not directly related to the Fermi level.

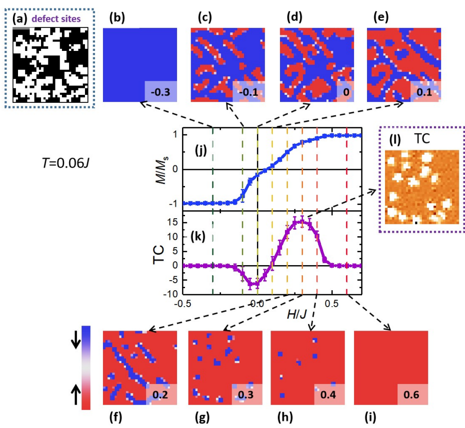

FIG. 4. (a) The binary image of the defect sites in the 32×32 spin sites. The white areas indicate the defect sites. (b)-(i) S_z images at various magnetic fields from $H/J = -0.3$ to 0.6. The field values are listed on the right bottom of the images. Red (blue) represents positive (negative) S_z. The colorbar scale is from -1 to 1. Magnetic bubble domains can be visualized during the magnetization reversal process. (j) The normalized magnetization (M/M_{S}), averaged over 128 different defect configurations, transition from -1 to 1 over a spread of increasing magnetic fields; error bars represent a single standard deviation across disorder configurations. (k) Field-dependent, disorder-averaged topological charge (TC) shows an antisymmetric profile; errors bars give a standard deviation. The dashed lines correspond to the magnetic fields at which the S_z images were simulated. (l) Real-space map of topological charge density at the TC maximum $H = 0.3J$. The image indicates that the topological charge density is concentrated on the magnetic bubbles.

To confirm that the THE does indeed arise from a defect-driven chiral domain wall mechanism, we perform Monte Carlo (MC) simulations of a 2D spin lattice [22]. The simulation qualitatively reproduces the domain behavior during magnetization reversal that is observed in the experiment. Fig. 4(a) shows a typical defect configuration. Figs. 4(b)-(i) show the simulated domain configuration across the reversal. As expected, reversed bubble domains (red bubbles) first emerge on nucleation defects, then expand and coalesce to form larger interconnected domains. Eventually, only a few unreversed bubble domains (blue bubbles) persist, until they finally flip at the end of the reversal process. The simulated domain behavior is in good agreement with the experimental observations shown in Fig. 2. The real-space distribution of TCs shown in Fig. 4(l) demonstrates that TC density concentrates at the curved domain walls of magnetic bubbles, and each such bubble carries a single TC. The random distribution of defects breaks up what might otherwise nucleate as one single-domain bubble into many disconnected bubbles, each of which can contribute its own TC. So long as a nonzero DMI is present to fix a domain wall chirality, each of these disconnected bubbles adds an additional TC to the system. By this mechanism, the MC simulation suggests that random defects in the presence of DMI lead directly to higher topological charge density. The total TC changes from negative to positive near zero magnetization as shown in Fig. 4(k), in good agreement with observed THE shown in Fig. 2(j) and Fig 3. MC simulations also reproduce the asymmetric peaks, likely due to the different kinetic barriers. Thus, it is possible to control the sign of THE by defect engineering.

The chiral-bubble-induced TCs also persist to higher temperatures. The TC density reaches maximum near $T = 0.2J$ as more magnetic bubbles form due to enhanced thermal fluctuations [22]. As the temperature rises, the TC peaks become more symmetric, consistent with the experimental results shown in Fig. 2. MC simulations at various temperatures qualitatively reproduce the crossover from the chiral-bubble mechanism to the spin chirality fluctuation mechanism [22]. We note that the same simulation parameters produce TC driven by spin chirality fluctuations (at $T \approx T_{\mathrm{C}}$) and chiral bubbles (at $T \ll T_{\mathrm{C}}$) in the same 2D uniaxial ferromagnet with DMI.

To confirm the topological Hall transport due to the emerging gauge field, we carry out Kubo formula calculations of the simulated spin texture of domains during the magnetization reversal [22]. The field-dependence of the Hall conductivity nicely follows the evolution of TCs, reproducing both negative and positive peaks [22]. The agreement further corroborates the notion that the THE is a sensitive probe of the gauge field emerging from chiral spin texture in 2D magnets.

In conclusion, we observed both positive and negative THE signals in a VST thin film system after suppressing the AHE. MFM imaging and MC simulations reveal that these signals originate from the nucleation and pinned magnetic bubbles arising during magnetization reversal. MC simulations and transport calculations confirm the existence of a THE due to the emergent gauge field (associated with TC) at the chiral domain walls of these bubble domains. Therefore, our results suggest that chiral-bubble-induced THE is a common phenomenon in ultrathin magnetic films and 2D ferromagnets with DMI.

However, the THE in such ferromagnetic systems is often overwhelmed by the AHE, and is thus hidden in the AHE loop. To reveal the intrinsic THE, the AHE must be carefully characterized and separated. Our work suggests that magnetic imaging techniques such as MFM could be an alternative method for characterizing the $M(H)$ loop in ultrathin film systems. The chiral-bubble mechanism not only provides a general explanation of the observed THE in many ferromagnetic thin films and heterostructures, but also opens the door to control and manipulation of topological transport via magnetic domain engineering.

The work at Rutgers is supported by the Office of Basic Energy Sciences, Division of Materials Sciences and Engineering, US Department of Energy under Award numbers DE-SC0018153. The work at CMU was supported by the Defense Advanced Research Projects Agency (DARPA) program on Topological Excitations in Electronics (TEE) under grant number D18AP00011. The work at Penn State is supported by ARO Young Investigator Program Award No. W911NF1810198 and the Gordon and Betty Moore Foundation's EPiQS Initiative (Grant GBMF9063 to C.-Z. Chang). The work at UNH is supported by Office of Basic Energy Sciences, Division of Materials Sciences and Engineering, US Department of Energy under Award number DE-SC0020221.

* Corresponding author: wenbowang@ucsb.edu

† Corresponding author: wdwu@physics.rutgers.edu

[1] X. G. Wen, F. Wilczek, and A. Zee, Phys. Rev. B **39**, 11413 (1989).

[2] J. W. Ye, Y. B. Kim, A. J. Millis, B. I. Shraiman, P. Majumdar, and Z. Tesanovic, Phys. Rev. Lett. **83**, 3737 (1999).

[3] Y. Taguchi, Y. Oohara, H. Yoshizawa, N. Nagaosa, and Y. Tokura, Science **291**, 2573 (2001).

[4] Y. Machida, S. Nakatsuji, S. Onoda, T. Tayama, and T. Sakakibara, Nature **463**, 210 (2010).

[5] A. Neubauer, C. Pfleiderer, B. Binz, A. Rosch, R. Ritz, P. G. Niklowitz, and P. Boni, Phys. Rev. Lett. **102**, 186602 (2009).

[6] J. Zang, M. Mostovoy, J. H. Han, and N. Nagaosa, Phys. Rev. Lett. **107**, 136804 (2011).

[7] N. Kanazawa, Y. Onose, T. Arima, D. Okuyama, K. Ohoyama, S. Wakimoto, K. Kakurai, S. Ishiwata, and Y. Tokura, Phys. Rev. Lett. **106**, 156603 (2011).

[8] S. X. Huang and C. L. Chien, Phys. Rev. Lett. **108**, 267201 (2012).

[9] W. Wang, M. W. Daniels, Z. Liao, Y. Zhao, J. Wang, G. Koster, G. Rijnders, C.-z. Chang, D. Xiao, and W. Wu, Nat. Mater. **18**, 1054 (2019).

[10] K. Yasuda, R. Wakatsuki, T. Morimoto, R. Yoshimi, A. Tsukazaki, K. S. Takahashi, M. Ezawa, M. Kawasaki, N. Nagaosa, and Y. Tokura, Nat. Phys. **12**, 555 (2016).

[11] J. Matsuno, N. Ogawa, K. Yasuda, F. Kagawa, W. Koshibae, N. Nagaosa, Y. Tokura, and M. Kawasaki, Sci. Adv. **2**, e1600304 (2016).

[12] C. Liu, Y. Y. Zang, W. Ruan, Y. Gong, K. He, X. C. Ma, Q. K. Xue, and Y. Y. Wang, Phys. Rev. Lett. **119**, 176809 (2017).

[13] D. Zhao, L. Zhang, I. A. Malik, M. Liao, W. Cui, X. Cai, C. Zheng, L. Li, X. Hu, D. Zhang, J. Zhang, X. Chen, W. Jiang, and Q. Xue, Nano Res. **11**, 3116 (2018).

[14] G. Chen, J. Zhu, A. Quesada, J. Li, A. T. NDiaye, Y. Huo, T. P. Ma, Y. Chen, H. Y. Kwon, C. Won, Z. Q. Qiu, A. K. Schmid, and Y. Z. Wu, Phys. Rev. Lett. **110**, 177204 (2013).

[15] S. Emori, U. Bauer, S.-M. Ahn, E. Martinez, and G. S. D. Beach, Nat. Mater. **12**, 611 (2013).

[16] W. Jiang, P. Upadhyaya, W. Zhang, G. Yu, M. B. Jungfleisch, F. Y. Fradin, J. E. Pearson, Y. Tserkovnyak, K. L. Wang, O. Heinonen, S. G. Te Velthuis, and A. Hoffmann, Science **349**, 283 (2015).

[17] N. Nagaosa and Y. Tokura, Nat. Nanotechnol. **8**, 899 (2013).

[18] J. Jiang, D. Xiao, F. Wang, J. H. Shin, D. Andreoli, J. X. Zhang, R. Xiao, Y. F. Zhao, M. Kayyalha, L. Zhang, K. Wang, J. D. Zang, C. X. Liu, N. Samarth, M. H. W. Chan, and C. Z. Chang, Nat. Mater. **19**, 732 (2020).

[19] L. Wang, Q. Feng, H. G. Lee, E. K. Ko, Q. Lu, and T. W. Noh, Nano Lett. **20**, 2468 (2020).

[20] K. M. Fijalkowski, M. Hartl, M. Winnerlein, P. Mandal, S. Schreyeck, K. Brunner, C. Gould, and L. W. Molenkamp, Phys. Rev. X **10**, 011012 (2020).

[21] F. Wang, X. Wang, Y.-F. Zhao, D. Xiao, L.-J. Zhou, W. Liu, Z. Zhang, W. Zhao, M. H. W. Chan, N. Samarth, C. Liu, H. Zhang, and C.-Z. Chang, arXiv:2004.12560 (2020).

[22] See Supplemental Material at ?? for full dataset and supporting data.

[23] W. Wang, C. Z. Chang, J. S. Moodera, and W. Wu, npj Quantum Mater. **1**, 16023 (2016).

[24] D. Xiao, J. Jiang, J. H. Shin, W. B. Wang, F. Wang, Y. F. Zhao, C. X. Liu, W. D. Wu, M. H. W. Chan, N. Samarth, and C. Z. Chang, Phys. Rev. Lett. **120**, 056801 (2018).

[25] L. Vistoli, W. B. Wang, A. Sander, Q. X. Zhu, B. Casals, R. Cichelero, A. Barthelemy, S. Fusil, G. Herranz, S. Valencia, R. Abrudan, E. Weschke, K. Nakazawa, H. Kohno, J. Santamaria, W. D. Wu, V. Garcia, and M. Bibes, Nat. Phys. **15**, 67 (2019).